Probing the electronic and geometric structures of photoactive electrodeposited Cu_2O films by X-ray absorption spectroscopy

Meltem Yilmaz [a,b], Albertus Denny Handoko [b,*], Ivan P. Parkin [a], Gopinathan Sankar [a,*]

[a] *Dept. of Chemistry, University College London, 20 Gordon St., London WC1H0AJ, UK*
[b] *Institute of Materials Research and Engineering, Agency for Science, Technology and Research (A*STAR), 2 Fusionopolis Way, #08-04 Innovis, 138634, Singapore*

ARTICLE INFO

ABSTRACT

Cu_2O is an attractive photocathode for important renewable energy reactions such as water splitting and CO_2 reduction. Electrodeposition is commonly used to deposit Cu_2O films on conductive substrates due to its simplicity and consistency. However, structural descriptors, linking electrodeposition parameters, film structure and the catalytic properties are elusive. A variety of Cu_2O films reported by many research groups would often display vastly different electronic properties and catalytic activity, while appear indistinguishable under common characterisation tools. In this work, we take a systematic look into electrochemically deposited Cu_2O and investigate the impact of deposition parameters towards the bulk and surface chemistry of the deposited film. Specifically, we employ high resolution XANES for thorough quantitative analysis of the Cu_2O films, alongside more common characterisation methods like XRD, SEM and Raman spectroscopy. Photoelectrochemical (PEC) studies reveal an unexpected trend, where the highest PEC activity appears to correlate with the amount of Cu^{2+} content. Other factors which also affect the PEC activity and stability are film thickness and crystallite grain size. Our study shows that the use of high resolution XANES, though not perfect due to possible self-absorption issue, is apt for extracting compositional descriptor in concentrated thin film samples from the pre-edge energy position analysis. This descriptor can serve as a guide for future development of more active Cu_2O based films for wide range of PEC processes as well as for solar cell applications.

1. Introduction

Developing new materials which can efficiently harness and utilise solar energy for renewable fuel production is of environmental and global interest. Photoelectrochemical (PEC) water splitting using solar light for hydrogen production has been one of the most studied approaches in this field [1]. Cuprous oxide (Cu_2O), a relatively non-toxic and abundant material with a direct bandgap of about 2 eV is a very attractive material for PEC water splitting. Its narrow bandgap allows the absorption of most visible photons, while its band positions are favourable for the hydrogen evolution reaction as the conduction band (CB) lies 0.7 V negative of the hydrogen reduction potential and the valence band (VB) just positive of the oxygen evolution potential [2]. Under a simulated sunlight (AM 1.5) it is predicted to have a maximum theoretical photocurrent of *ca.* -15 mA cm^{-2} and 18% solar to hydrogen (STH) efficiency [3]. One major setback for using Cu_2O as a photo-

cathode is photocorrosion, as its redox potentials lie within the bandgap. Protection strategies to minimise this photocorrosion have included deposition of metal oxide nanolayers via atomic layer deposition (ALD) [3,4] and co-catalyst deposition [5–7].

Cuprous oxide thin films have previously been prepared via various methods including physical vapour deposition [8–10], chemical vapour deposition [11–14], hydrothermal [15], and electrodeposition [16–18]. Among these methods, electrodeposition is arguably the most versatile and cost-effective as it doesn't require high vacuum equipment and can be easily scaled. However, structural or compositional descriptors linking electrodeposition parameters, film structure and the catalytic properties are elusive, holding back the development of Cu_2O based photo/electrocatalysts. Anodic formation of Cu_2O in aqueous solutions has been proposed to proceed through soluble Cu^+ species [19]. Similarly, cathodic deposition of Cu_2O involves an initial reduction of Cu^{2+} precursors to soluble Cu^+ species, followed by Cu_2O nucleation when the local Cu^+ concentration is beyond the solubility limit [20]. The 2-step reaction involving multiple Cu species suggests that Cu_2O formation is likely to be sensitive to the type of anion or reducing additives present [21], pH [22], and other factors that

affect Cu species solubility. Indeed, small changes in the deposition parameters, including supporting electrolyte, pH, temperature, time, and applied voltage have been shown to significantly alter the electronic and photochemical properties of electrodeposited Cu_2O [20,22–26]. A majority of these studies rely on common and more accessible tools to characterise electrodeposited Cu_2O films such as electron microscopy, X-ray diffraction (XRD), X-ray photoelectron spectroscopy (XPS) and Raman spectroscopy. Although useful to certain extent, these analytic tools struggle to detect and quantify minute presence of various Cu oxidation states. X-ray absorption spectroscopy (XAS) studies can determine Cu oxidation states. However, the resolution offered in conventional XAS setup is not sufficient to determine low concentrations of mixed Cu species.

In this study, we show that high resolution XAS, available at certain synchrotron radiation centralised facilities, can complement laboratory accessible tools in providing insight into the structures of electrodeposited Cu_2O films and relate it to the activity as photocathodes. High resolution XAS methods are very widely used for powder based catalysts [27,28], but very few studies have been conducted for film-based catalysts [29]. It is striking to find that the presence of small amounts of Cu^{2+} species is correlated to the enhanced photocatalytic activity of our electrodeposited Cu_2O photocathodes, albeit at the expense of the stability. We believe Cu^{2+} fraction can serve as compositional descriptor to further our understanding of how structure and composition relates to the performance of a photocathode for PEC water splitting and highlight the importance of XAS in catalysts characterisation and optimisation.

2. Experimental

2.1. Cu_2O electrodeposition

Electrodeposition was carried out using a lactate stabilised electrolyte bath solution. This solution consisted of 0.2 M $CuSO_4 \cdot 5H_2O$ (Sigma-Aldrich ACS reagent, $\geq$98.0%) and 1.5 M lactic acid (Sigma-Aldrich, 85% solution). The pH of the solution was then adjusted using 5 M NaOH (Alfa-Aesar, 97%) to maintain it between 11.0 and 11.3. Prior to use, the fluorine doped tin oxide (FTO) substrates (Tech 15, Sigma-Aldrich) were cleaned via sequential sonication in acetone, isopropyl alcohol, methanol and deionised water for 15 min each. The electrodeposition was carried out using a three-electrode set up using, with fluorine doped tin oxide (FTO) coated glass (sized 2 × 1 cm), platinum mesh (Goodfellow) and Ag/AgCl (3 M NaCl, BASi Inc.) as the working electrode, counter electrode and reference electrode respectively. The bath solution temperature was maintained at 63–65 °C, after which electrodeposition was carried out potentiostatically. Two deposition potentials were selected based on the linear sweep voltammogram of the electrolyte bath at 65 °C (*Fig. S1*) [30] and the Pourbaix diagram for the Cu, Cu_2O and CuO system [25].

Once the desired electrodeposition period was over, the substrates were washed with deionized water and left to dry in air.

Table 1
Summary of the parameters varied to grow Cu_2O films, followed by labels assigned to each film, where the deposition potentials are with respect to Ag/AgCl reference electrode.

Deposition time (mins)	Deposition potential	
	−0.4 V	−0.5 V
2	402	502
10	410	510
30	430	530
60	460	560

A summary of the deposition parameters used in this study is given in Table 1. The sample names refer to the potential and time. For example, the sample name *402* refers to films deposited at −0.4 V vs Ag/AgCl for 2 min.

2.2. Materials characterisation

Various characterisation methods have been employed in this study to elucidate the exact structure of the films. X-ray diffraction (XRD) was utilised for phase identification using a Bruker D8 diffractometer with parallel beam and grazing incidence angle optics equipped with Cu $K\alpha_{1+2}$ source powered at 40 kV, 40 mA and coupled with a LynxEye silicon strip detector. Scans were performed with an incidence angle of 1° using a 0.05° step for 1 s/step. Raman spectra were collected with a Renishaw inVia confocal Raman microscope equipped with a 514.5 nm wavelength laser. Electron micrographs were collected using a JEOL 6701 SEM with secondary electron imaging and accelerating voltage of 5 kV to image samples. Particle sizes and film thicknesses were measured using the ImageJ software (version 1.52a).

UV–vis spectra were collected using a PerkinElmer Lambda 950 spectrometer in the transmission mode. Subsequently, optical band gaps, E_g, of the films were determined using the *Tauc* relation:

$$(\alpha h\nu)^2 = A(h\nu - E_g) \tag{1}$$

where α is the absorption coefficient, $h\nu$ is the photon energy, A is a constant describing the band tailing parameter and E_g is the optical band gap. Accordingly, a *Tauc* plot of $(\alpha h\nu)^2$ versus $h\nu$ is obtained, which yields the band gap when the straight-line portion is extrapolated to the energy axis.

The chemical states of the surface species have been measured using X-ray photoelectron spectroscopy (XPS) and Auger electron spectroscopy (AES) on a Thermoscientific K-alpha spectrometer equipped with a monochromatic Al $K\alpha$ X-ray source. Analysis was carried out using Casa XPS software (version 2.3.19). The adventitious C $1\,s$ peak was calibrated at 284.8 eV and used as an internal standard to compensate for charging effects.

The chemical environment of the Cu species in the Cu_2O films was probed using X-ray absorption spectroscopy (XAS). High energy resolution fluorescence X-ray absorption near edge structure (HERFD-XANES) experiments were conducted on beamline I20-Scanning at the Diamond Light Source [31]. This beamline uses a four-bounce monochromator, operating with Si(1 1 1) crystals, with an energy resolution of $\Delta E/E = 1.3 \times 10^{-4}$. The resulting beam size on the sample is 400 × 300 μm (H × W). The incident energy was scanned between 8820 and 9400 eV, with a step size of 0.3 eV in the XANES region. A Rh coated collimating mirror was used with subsequent harmonic rejection using a Si coated mirror. The X-ray emission energy was selected using a Johan-type spectrometer with 1 m diameter Rowland circle and equipped with 3 spherically bent analyser crystals for fluorescence measurements. The edge position reproducibility is better than ± 0.1 eV for the monochromator used at this beamline,[31] signifying that any shift over this value should be considered as a genuine change with respect to the chemical change. Pellets containing evenly mixed 96 wt% cellulose and 4 wt% reference materials of CuO (Sigma-Aldrich, 99.999% trace metal basis) and Cu_2O (Sigma-Aldrich $\geq$ 99.9%) and their physical mixtures were also measured to aid further analysis and comparison. Data processing was carried out on the computer software package Athena and Artemis (Demeter version 0.9.26) [32]. This was initially done by selecting the edge position E_0 as a fraction of the edge step, followed by edge step normalisation. Normalisation involved extrapolation of the pre-edge line to all energies in the measured range of the data and subtracting this from μ(E).

Finally, the resulting data was divided by the normalisation constant, $\mu_0(E_0)$.

2.3. Photoelectrochemical performance measurements

The PEC properties were investigated in a conventional three-electrode cell using an electrochemical analyser (IVIUM Technologies, CompactStat.h standard). The as-prepared film, a Pt mesh and an Ag/AgCl electrode were used as the working, counter and reference electrodes, respectively. Sunlight was simulated with a 150 W xenon lamp (Newport) fitted with AM 1.5 filter (Newport). The light intensity was set to 1 Sun using a custom-made calibrated crystalline silicon solar cell, equivalent to global AM 1.5 illumination at 100 mW cm^{-2}. The photocurrent of the samples was measured in 0.5 M Na$_2$SO$_4$ solution (pH = 5.8) under constant stirring. Samples were illuminated from the back side (FTO substrate side) with an opaque mask to allow a defined irradiated area of 0.26 cm^2. Linear sweep voltammetry (LSV) was performed under manual light chopping at a scan rate of 10 mV s^{-1} in the cathodic direction between 0 and -0.6 V vs Ag/AgCl. Cyclic voltammetry (CV) measurements were performed using the same scan rate and potential range, with the omission of the light chopping procedure.

The potentials of all PEC measurements in this work are reported against the reversible hydrogen electrode (RHE), which have been calculated by using the Nernst equation:

$$E_{RHE} = E^0_{Ag/AgCl} + E_{Ag/AgCl} + 0.059 * pH \tag{2}$$

where E_{RHE} is the converted potential versus RHE, $E^0_{Ag/AgCl}$ = 0.1976 at 25 °C, and $E_{Ag/AgCl}$ is the experimentally measured potential against Ag/AgCl reference electrode.

3. Results and discussions

3.1. Basic materials characterisation

The as-deposited films appear translucent or opaque depending on the deposition conditions and dark orange in appearance, with a pale white top layer (*Fig. S2*). We first examine the as-deposited films with laboratory-based characterisation tools of SEM, XRD, Raman spectroscopy and XPS. The electron micrographs for the films deposited at the two potentials show similarities in the morphology, mostly composed of initial cubic crystals at lower deposition times, with some cubic-pyramidal integrated structures dominating at longer times (Fig. 1).

Siegfreid *et al.* [21] have reported similar shape transformations for films electrodeposited in solutions containing SO$_4^{2+}$. However, one interesting feature which can be inferred from these electron micrographs is that the deposition rate at -0.5 V is faster than at -0.4 V. The substrate is not fully covered when deposition takes place at -0.4 V for 2 min (Fig. 1*a*), in contrast to the film deposited at -0.5 V for the same deposition time (Fig. 1e). This may be due to the different electron transfer kinetics and the corresponding activation energy at the Cu$_2$O-solution interface during film growth, which correlates to a temperature dependant limiting current [25]. Homogenous coverage seems to be reached at both potentials by the 10th minute (Fig. 1*b, f*). Expectedly, the average film thicknesses and particle sizes (*Fig. S4*) increase with longer deposition time for both potentials.

The XRD patterns of the films (Fig. 2) showed highly crystalline cuprite structure for all eight films synthesised, with a predominant out of plane orientation of (1 1 1). This suggests that the more desirable *p*-type Cu$_2$O has been formed [33]. The films deposited at shorter times for both deposition potentials showed more prominent substrate peaks, probably due to the relatively thinner nature of these films. We note that neither CuO nor Cu metal were detected from the XRD patterns.

The characteristic phonon frequencies of crystalline Cu$_2$O (218, 308 cm^{-1} 2nd order overtone; 515 cm^{-1} Raman active mode; 409 cm^{-1} 4th order overtone; 629 cm^{-1} infrared active mode) [34–36] are present in the Raman spectra of all samples (Fig. 3*and Fig. S5*), corroborating the XRD results. Although the Raman peak positions are the same for each sample, we note that the peak intensities vary with increasing deposition times. In general, samples synthesised with shorter electrodeposition time show relatively higher intensities. As Raman intensity is a function of polarizability and symmetry [37], we speculate that its attenuation on films grown at longer deposition times may be an indication of symmetry reduction.

The optical bandgaps estimated using *Tauc* relation of UV–Vis absorption data (*Figs. S6 and S7*) appear to be consistent with the literature, where values of 2.0 to 2.4 eV have been commonly reported [38]. We note that the bandgap seems to be narrowing with longer electrodeposition time. Narrower optical bandgap has been linked to nanosized grain, stress/strain and presence of impurities/defects [39]. In our case, stress/strain or impurities/defect could be more likely causes as the grains are too large to induce nano-confinement effects (Fig. 1).

The surface structure of all eight films was also probed using XPS and Auger spectroscopy. Although XPS and AES are very effective in identifying and quantifying various elemental species, Cu is
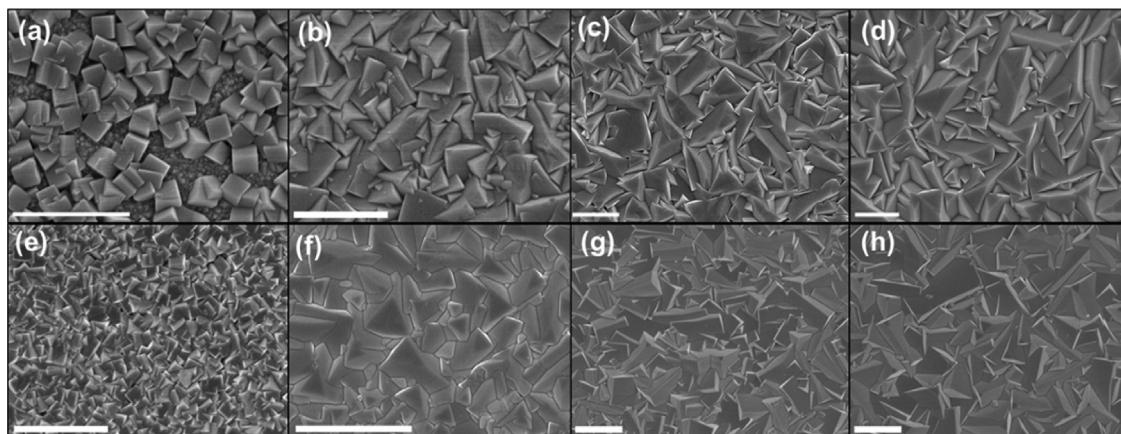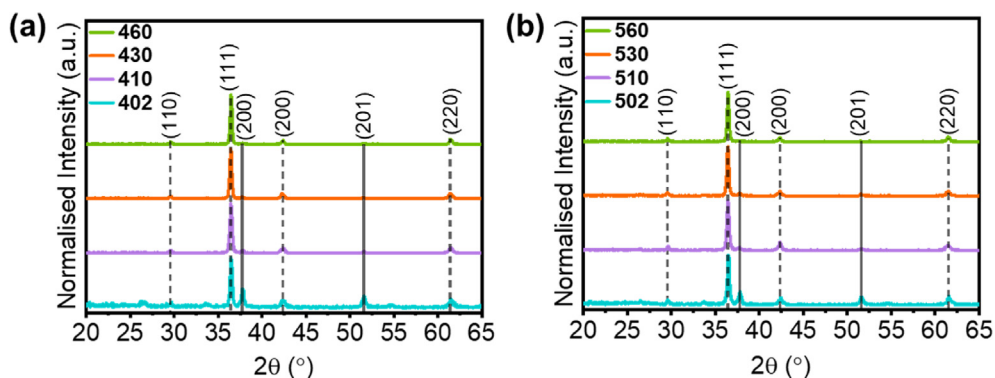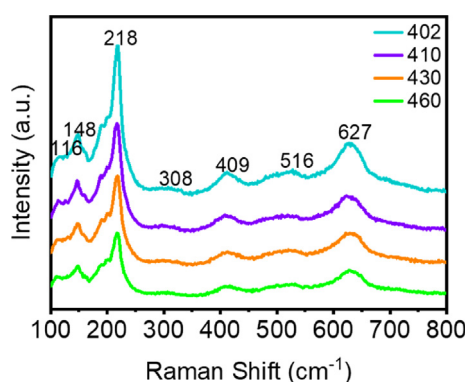

Fig. 1. Top-view SEM images of (a) 402, (b) 410, (c) 430, (d) 460, (e) 502, (f) 510, (g) 530 and (h) 560. All the scale bars indicate 2 μm.

Fig. 2. XRD pattern of films deposited at a constant potential of (a) −0.4 V and (b) −0.5 V. The dotted peaks refer to the Cu_2O peaks (PDF file No. 05-0667) and the solid lines refer to the FTO substrate peaks (PDF file No. 41-1445).

Fig. 3. Raman spectra of films deposited at a constant potential of −0.4 V and using a 514.5 nm laser source.

a particularly difficult element to analyse as the binding energies of the three oxidation species are very close to one another [40]. The shake-up satellite peaks in the Cu 2p spectra are often used as an indication of the presence of Cu^{2+} species [41–44]. However, quantitative analysis using these satellite peaks were difficult because very precise constraints are needed to fit these peaks. A good fit was not obtained as the shake-up peak sizes were very small, significantly increasing the fitting error [45]. Curve fitting was done for the Cu 2p spectra (excluding the shake-up satellite peaks) of sample 460 (Fig. 4**a**). Quantification of the different Cu species was attempted by comparing the ratios of the areas of the Cu

$2p_{3/2}$ peaks (**Table S1**). We observe no consistent connection between deposition parameters and Cu species quantification obtained using XPS, which may stem from measurement or fitting inaccuracy or rapidly changing surface state of the sample during handling.

Previous studies have shown that the Cu LMM spectral line shapes could provide a clearer method of Cu species differentiation [45–47]. Fig. 4**b** shows the Cu LMM spectra for the −0.4 V deposition series, whilst the corresponding figure for the −0.5 V deposition series is presented in **Fig. S8b**. All films showed a peak at a kinetic energy of *ca.* 916.5 eV or lower, which indicates that the majority of the film surface consists of Cu_2O [46].

3.2. X-ray absorption spectroscopy

While basic characterisation methods are useful in confirming the identity of the films, they were ineffective in detecting the precise oxidation state in our electrodeposited Cu_2O samples. Beyond the expected variation in grain size and film thickness, all eight films, show almost identical XRD, Raman, XPS and Auger profile.

All eight films were investigated using high-energy resolution fluorescence detected X-ray absorption near edge structure (HERFD-XANES) spectroscopy at the Cu K-edge. Cu^0 foil and two known reference compounds, CuO and Cu_2O (to represent Cu^+ and Cu^{2+} species respectively), were also measured (**Fig. S9**). HERFD-XANES is highly sensitive in detecting minute changes in oxidation states as reflected on the pre-edge or edge position and curve shape. The peak at the rising absorption edge around 8980.41 eV in Cu^0 foil sample (termed peak B0) is attributed to
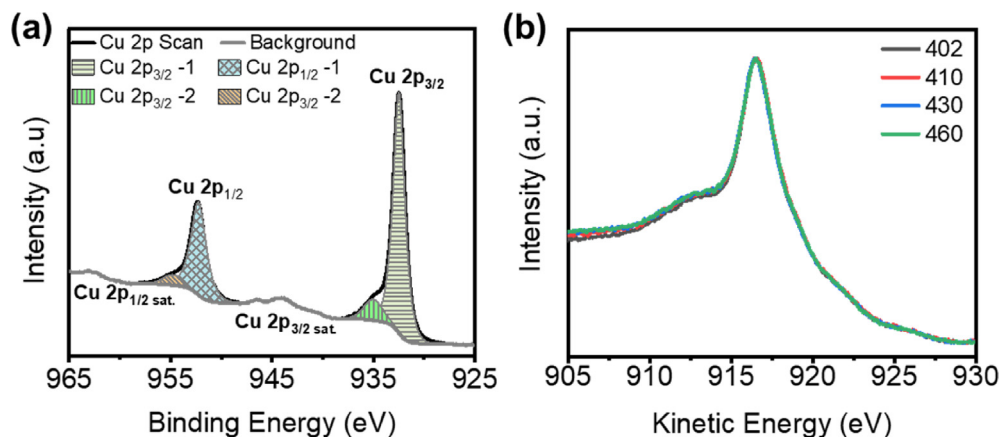
Fig. 4. (a) Cu 2p XPS fitting for sample 460 and (b) Auger spectra of Cu LMM for samples deposited at −0.4 V.

the $1s \rightarrow 4p$ electric dipole allowed transition (**Fig. S9b**) [48]. In Cu_2O reference compound, a sharper peak around 8981.41 eV (termed peak B) is attributed to the $1s \rightarrow 4p_{xy}$ transition, followed by a peak around 8995.77 eV (termed peak C) attributed to $1s \rightarrow 4p_z$ due to the ligand field effect. In contrast, CuO reference compound shows a weak characteristic pre-edge peak caused by the electric quadruple allowed 1s → 3d transition [49] at 8977.96 eV (termed peak A), followed by the $1s \rightarrow 4p_{xy}$ peak (8985.43 eV, termed peak B2) and the $1s \rightarrow 4p_z$ peak (8997.30 eV, termed peak C2), at much higher energy than peaks B and C of Cu_2O species. Two different approaches were then used to quantify the fractions of Cu phases in the electrodeposited film samples: (1) carrying out a linear combination fitting (LCF) analysis, and (2) tracking the peak position in the rising absorption edge (peak B).

As a first approach, LCF analysis was carried out within an energy range of −20 eV to +30 eV of the edge energy. LCF has been successfully used to estimate the species changes in oxidation state, as it is embedded inside Athena software and fairly straightforward to implement [50–52]. LCF analysis fits the XAS spectra position within the specified energy range to a model spectrum created by linear interpolation of Cu^+ and Cu^{2+} reference compounds, in our case Cu_2O and CuO. An example of an LCF fit for sample 502 is presented in **Fig. S10**, and the resulting least squares fitting data is presented in Table 2 as estimated fraction of Cu^{2+}.

The outcome of the LCF analysis shows that samples grown at longer electrodeposition times (samples 460, 530 and 560) closely match the Cu_2O reference compound. The low goodness of fit parameters, R-factor and reduced χ^2 (<0.00511 and < 0.00128 respectively, **Table S2**) show that reasonable fit was achieved. Overall, the LCF approach suggests that films deposited at −0.4 V has slightly higher Cu^{2+} fraction compared to those deposited at −0.5 V. Decreasing amounts of Cu^{2+} with increasing electrodeposition time was observed, *e.g.* from 11.4% for 2 mins at −0.4 V to 0% after 60 mins. Although a useful method, reservations have been identified as LCF entirely relies on the suitability of the reference compounds to adequately represent the material desired. In addition, self-absorption processes may hinder the fitting procedure [53]. In this study, LCF appears to struggle in clearly distinguishing thicker samples to pure Cu_2O, possibly due to self-absorption issue. However, it does provide a trend in the fraction of species present in the system.

As the LCF approach appears to be limited in examining the thicker samples, we turn our focus to the edge energy shift analysis. A clear shift in the rising absorption edge and edge position is observed upon varying the deposition potentials and the deposition times (Fig. 5). Closer examination of the edge features of the films indicate that *none* of the films are pure Cu_2O, but rather they contain minute amounts of Cu^{2+} species. This key information was not observed in any of the basic characterisation results.

The energy positions of the rising absorption edge on our film samples (peak B), are then tracked and analysed at half the fraction

of the edge step, $0.5X\mu(E)$ (Fig. 6). Interestingly, films synthesised with longer electrodeposition times show lower energy positions, indicative of diminishing amounts of Cu^{2+} species as the film grows thicker. Comparing the two deposition potentials, films synthesised at −0.4 V overall have higher peak B energies at $0.5X\mu(E)$, which can be interpreted that these films have higher amounts of Cu^{2+} species in their bulk structure. Furthermore, film 402 has the highest energy at $0.5X\mu(E)$, suggesting that it has the highest fraction of Cu^{2+} species among all 8 samples analysed here. There is no evidence for the presence of metallic copper as the peak B energy for Cu^0 at $0.5X\mu(E)$ lies at a lower energy than the oxides.

A quantitative analysis can then be carried out using the variation in the peak B energy at $0.5X\mu(E)$ assuming the linear relationship of Vegard's law [54] (*Eq. (3)*):

$$Edge_{film} = x\ Edge_{Cu}^{2+} + (1-x)\ Edge_{Cu}^{+} \tag{3}$$

Rearrangement of this relation for x reveals the approximate amounts of Cu^{2+} species. Here, we note that this calculation using $Edge_{Cu}^{2+}$ is based on the CuO reference compound. Although a reasonable assumption, it should be noted that other Cu^{2+} compounds such as $Cu(OH)_2$ may also be present in the films. $Cu(OH)_2$ has an even higher edge energy shift (between 8984 and 8987 eV) [55] with respect to Cu_2O. This shift in edge energies for Cu^{2+} compounds has been attributed to different local site geometry such as square planar or distorted octahedra [56,57]. However, it is difficult to definitively determine which Cu^{2+} species are present in our samples. For this reason, we interpret the estimation of Cu^{2+} amounts in our films with caution, assuming CuO to be the likely phase. Higher amounts of Cu^{2+} species are observed in the thinner films, with sample 402 having the highest approximate amount of 6.85% Cu^{2+} (Table 2), similar to the initial prediction using LCF analysis. We recognise that the peak B energy shift with electrodeposition time were not strictly linear (Fig. 6) and deviations from Vegard's law are often observed [58]. Nonetheless, we found that it still provides useful approximations as an alternative method for quantifying the amounts of the varying Cu species in the films.

Apart from the position, the intensity of peaks B and C contains information about the molecular geometry. In compounds with linear 2-coordinated Cu complex like Cu_2O, peak B represents the $1s \rightarrow 4p_{xy}$ transition, while peak C represents $1s \rightarrow 4p_z$ [59]. Ideally, deviations from the centrosymmetry, including film orientation or compositional change, should be proportional to these peak intensities [60]. However, the prevalent self-absorption issue in our film samples, exacerbated with the thickness variation effects, prevents meaningful interpretation of the peak intensity trend. See **Figs. S11-12** and the accompanying text for further discussion.

One other method of confirming the presence of Cu^{2+} in the films is to analyse peak A, which is associated with the electronic quadrupole allowed 1s → 3d transition. This weak transition is not observed in the film samples, which we attribute to the very small amount of Cu^{2+} species with diverse local geometry around it, thus supressing this peak. Cu_2O-CuO physical mixture data is included in **Fig. S12d** to represent a controlled case where Cu^+ and Cu^{2+} are evenly distributed but are chemically separated from each other. In this ideal situation, a weak peak A around this region is only observed when the mixtures contain more than 5% CuO. The situation in the film samples are different to the physical mixture, as the Cu^{2+} structure can form as an interface next to Cu_2O [61]. Additionally, many forms of Cu^{2+} species can coexist in the film, as electrochemical deposition is known to introduce trapped ions or water molecules [62] thus changing the local environment. It is well documented that the intensity of the pre-edge peak A (similar to the edge shift as noted before) depends on the local geometry of the absorbing atoms [63–66]. For example, significant suppression of the 1s → 3d pre-edge transition is expected if the

Table 2
Estimations of Cu^{2+} fraction determined from LCF analysis and peak B position at $0.5X\mu(E)$.

Sample	Cu^{2+} fraction (%)	
	From LCF analysis	From peak B position
402	11.4	6.85
410	6.8	6.12
430	1.3	4.98
460	0	4.14
502	9.2	3.98
510	4.5	3.1
530	0	1.45
560	0	0.7
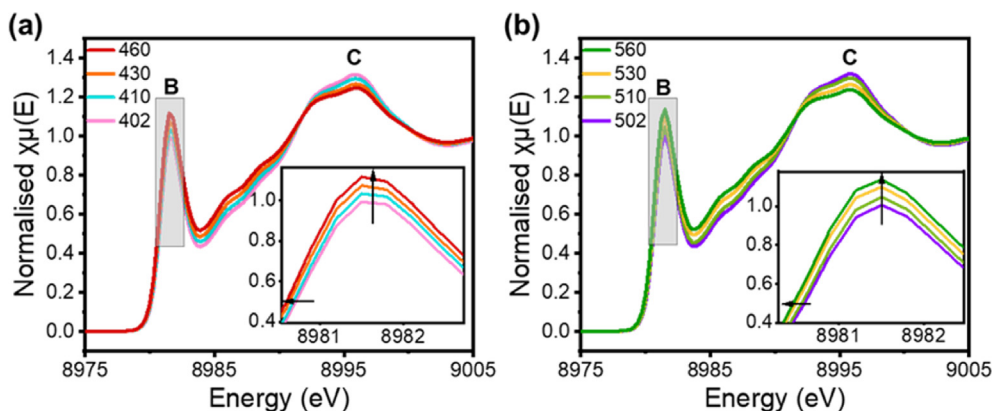
Fig. 5. Normalised high resolution XANES spectra measured at the Cu K-edge for films synthesised at (a) −0.4 V and (b) −0.5 V. Shaded box highlights the region shown in the inset. Arrows in the inset highlight the fine energy and intensity variation within peak B of these films.
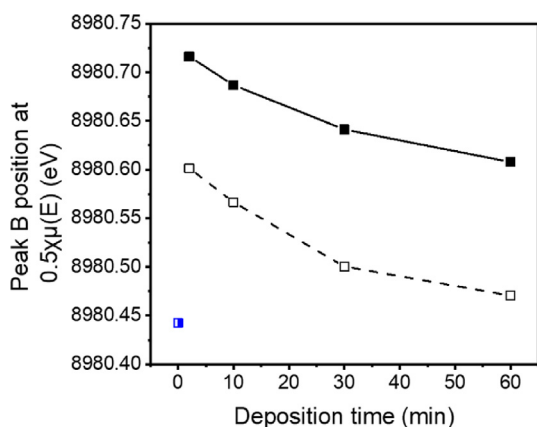
Fig. 6. Analysis of peak B position at 0.5Xμ(E) variation with deposition time for films synthesised at −0.4 V (filled) and −0.5 V (hollow). The data point with half-filled square represent the model Cu_2O reference material.

symmetry of a metal species changes from tetrahedral to octahedral [56]. Variation in the ligand field strength and slight changes in the dihedral angle between ligand-Cu-ligand planes also appears to impact the intensity and the energy of this peak [56].

Further, since no significant spectral changes were observed between samples, we also considered the possibility of whether the changes observed in the XANES were simply due to changes in the amount of copper as film thickness increases, leading to stoichiometric structural changes. Schedel-Niedrig *et al.* [67] have reported that (sub)stoichiometry could only be detected in surface oxidised single or polycrystalline copper within the first tens of Å using electron yield measurement in the soft X-ray range. Thus, spectral changes are only expected to arise from (sub)stoichiometric structures if the particles are nanosized (*ca.* 20 nm) or in extremely thin films, where the surface to bulk ratio of these species are significantly higher [68]. Our films neither have nanosized particles nor are extremely thin, therefore we can negate this possibility.

It is also possible to determine Cu^{2+} fraction through bond length analysis from the EXAFS fitting. However, it is not a suitable method in our case due to the limited *k*-range. This is because the determination of interatomic distances of Cu-O between Cu_2O and CuO phases (1.84 Å [69] and 1.95 Å [70] respectively) is around *ca.* 0.1 Å, which is less than the distance resolution that can be achieved with this data (***Fig. S13, Table S3***).

The methods used here have their merits and limitations, thus it is important to use them conjointly to gain a better understanding

of the structural chemistry of the films. For example, self-absorption can have a disproportionate effect on the LCF approach, especially for data collected in the fluorescence mode as in this study. This is mainly due to thicker samples being weighted more heavily toward the front of the sample, introducing a surface gradient [53]. This is because the LCF method uses a statistical approach to minimise the sum of the squares of the difference in between the data and the fit. Therefore, the accuracy of the fit with regards to the LCF depends on how well the reference compounds represent the components in the samples. In contrast, the Vegard's law is a linear relationship which assumes that the crystal structure of the constituent isolated elements is retained when in the solid solution. This assumption is often not fully representative of the exact film condition, thus deviations from the Vegard's law are observed.

3.2.1. Photoelectrochemical performance

The effects of deposition parameters on the PEC performance was evaluated using the method detailed in *section 2.3*. Light and dark currents were measured simultaneously under manually chopped irradiation. For clarity, we display the PEC data for the thinnest and thickest films of both −0.4 V and −0.5 V deposition series in Fig. 7, while the full results of all eight films can be referred to in ***Fig. S14***.

A plateau in the photocurrent is observed for films deposited at 2 and 10 min at both deposition potentials after about 0.1 V vs. RHE, although each film shows very different magnitudes of photocurrent. On first inspection, we observe that thinner films tend to show larger photocurrent, which lead to the speculation that the photocurrent attenuation may be related to the longer inelastic mean free path (IMFP) associated with a thicker film (Fig. 7**c**). However, IMFP difference alone could not explain the significant differences in films 402 and 502 that have very similar thickness (Fig. 7**a-b**).

In fact, films deposited at −0.5 V consistently display lower photocurrents than those deposited at −0.4 V with similar deposition time (film thickness). Incidentally, films grown at −0.4 V also show much higher Cu^{2+} amounts (Table 2), suggesting that Cu^{2+} presence is beneficial in photocurrent generation. Film 402 generated the highest photocurrent which also appears to have the highest Cu^{2+} presence, as determined form LCF analysis and pre-edge position analysis. CuO is the most likely Cu^{2+} species to form in the film which is intrinsically a *p*-type semiconductor. The narrow band gap of CuO (between 1.4 and 1.7 eV) aligns well with Cu_2O, providing additional light adsorption while inducing charge separation [38,71–74]. A higher amount of Cu^{2+} in the thinner films can then be correlated to longer lived photogenerated electrons,
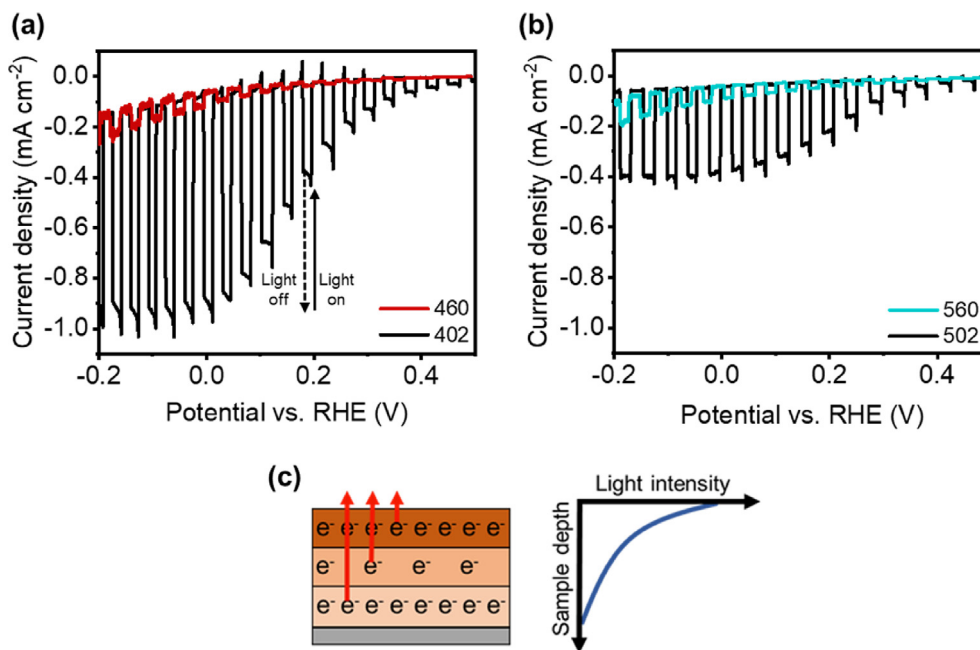
Fig. 7. Current density-potential (J-V) graphs for films (a) 402 and 460 and (b) 502 and 560 under chopped illumination. (c) Schematic diagram variation in light intensity as the sample depth changes. Electrons which are closest to the substrate have a longer IMFP to travel to the surface and carry out redox reactions at the solid electrolyte interface.

akin to the effect seen in Cu_2O/RuO_x junction structure [5,75,76]. As the films grow thicker, the Cu^{2+} presence effect is diminishing, presumably overwhelmed by the thickness/IMFP effect. For example film 410 has just slightly lower Cu^{2+} amount than 402 but its photocurrent is drastically lower. Additionally, the particles size effect could be a contributing factor. That is, at lower deposition times, particles are smaller thus a larger surface area is exposed to the electrolyte.

One other factor which could be contributing to the high photocurrent measured for film 402 is the formation of Schottky barriers at the semiconductor–metal interface (Cu^+- Cu^0) as the Cu_2O undergoes reductive decomposition during the PEC process according to equation:

$$Cu_2O + 2e^- + 2H^+ \rightarrow 2Cu + H_2O \qquad (7)$$
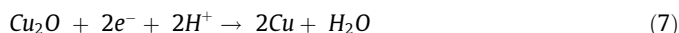
We posit that the *in-situ* formation of Cu^0 during the PEC process has similar effect of adding co-catalysts, which enhances photogenerated carriers separation and minimises recombination losses [77]. However, as Cu^0 is formed in the expense of Cu_2O, the photoabsorber, we see a gradual loss in photoactivity, leading to stability issues.

Apart from PEC activity, the stability of the Cu_2O films is also assessed by analysing the dark current profile across the chopped linear sweep (**Fig. S15**). Larger cathodic current in dark condition signifies poorer stability, as it is likely to originate from electrochemical Cu^+ or Cu^{2+} reduction and not hydrogen evolution reaction [78]. Here, we see that film 402, which shows the highest photocurrent, actually has the poorest film stability.

The lowest dark current is observed for the films deposited at 10 and 30 min at both potentials indicating higher stability. The stability of these films was further probed by using cyclic voltammetry (CV) (**Fig. S16**). Significant decay in the photocurrent due to reductive decomposition to Cu metal is observed with each light cycle for all films. However, the least amount of decay was observed for film 510. This film showed a 27% reduction in the photocurrent density at −0.05 V vs RHE in its forward cycle from 1st to the 5th CV cycle, whereas a 70% reduction was observed for the

least stable film, 402. Here, we see that the film 402 generates a high photocurrent at the expense of its stability. This observation agrees with the chopped linear sweep voltammetry results. A 6th CV cycle which was conducted in the dark following the 5 light CV cycles is also presented. The stability of the film 510 compared to the other films tested is revealed with the low dark current density, showing that the material is still photoactive following 10 min of light exposure. These preliminary PEC tests lead to the conclusion that the most stable film out of the 8 films was the one synthesised at −0.5 V for a deposition time of 10 min.

4. Conclusions

Cu_2O is and will be central to photo/electrocatalysis reactions that desires to operate under visible wavelengths due to its appropriate band structure. The advances in Cu_2O based photo/electrocatalysts are relatively slow due to elusive structural descriptor link to the catalytic activity, such that it is common to see seemingly identical samples synthesised by different researchers showing vastly different catalytic activity. Our study indicates that Cu^{2+} amount can be such descriptor. Positive detection of Cu^{2+} species on the films surface can be confirmed with XPS and AES measurements, although quantitative assessment of Cu^{2+} amounts using these two techniques proved to be arduous. HERFD-XANES, though not perfect due to possible self-absorption issues, is particularly appropriate to quantify minute amounts of Cu^{2+} species in concentrated thin film samples from the pre-edge energy position analysis. A series of HERFD-XANES quantitative analyses revealed that thinner electrodeposited films had higher fraction of Cu^{2+} species, which can be linked to their photoelectrocatalytic activity.

PEC measurements showed that having a higher amount of Cu^{2+} improved the photocurrent generated. However, this was at the expense of long-term stability due to more rapid reductive decomposition to Cu metal. We propose that the presence of Cu^{2+} species, specifically CuO, enhances light absorption and charge separation, thus increasing the photocurrent generated. Formation of Schottky barriers at the newly formed metal semiconductor contacts, as a

result of reductive decomposition of Cu_2O to metallic Cu, also increases the photocurrent. Nevertheless, this is limited by other factors including film thickness and crystallite grain size. We concluded that the film deposited at -0.5 V vs. Ag/AgCl for a period of 10 min, was the most stable in terms of its PEC performance. Quantitative analyses from XAS indicated that this film had a medium amount of Cu^{2+} in its structure, therefore a compromise between the Cu^{2+} amount and stability is observed. This work highlights the important role of XAS based techniques for future development of PEC active films for wide range of energy generation and conversion applications.

Declaration of Competing Interest

The authors declare that they have no known competing financial interests or personal relationships that could have appeared to influence the work reported in this paper.

Acknowledgements

Appendix A. Supplementary data

Notes and References

[1] S.D. Tilley, Recent Advances and Emerging Trends in Photo-Electrochemical Solar Energy Conversion, Adv. Energy Mater. 9 (2019) 1802877.

[2] P.E. De Jongh, D. Vanmaekelbergh, J.J. Kelly, Photoelectrochemistry of Electrodeposited Cu2O, J. Electrochem. Soc. 147 (2000) 486–489.

[3] A. Paracchino, V. Laporte, K. Sivula, M. Grätzel, E. Thimsen, Highly active oxide photocathode for photoelectrochemical water reduction, Nat. Mater. 10 (2011) 456–461.

[4] J. Azevedo et al., Tin oxide as stable protective layer for composite cuprous oxide water-splitting photocathodes, Nano Energy 24 (2016) 10–16.

[5] E. Pastor et al., Interfacial charge separation in Cu2O/RuOx as a visible light driven CO2 reduction catalyst, Phys. Chem. Chem. Phys. 16 (2014) 5922–5926.

[6] L. Pan et al., Boosting the performance of Cu2O photocathodes for unassisted solar water splitting devices, Nat. Catal. 1 (2018) 412–420.

[7] C.G. Morales-Guio, S.D. Tilley, H. Vrubel, M. Grätzel, X. Hu, Hydrogen evolution from a copper(I) oxide photocathode coated with an amorphous molybdenum sulphide catalyst, Nat. Commun. 5 (2014) 3059.

[8] S.H. Wee, P.-S. Huang, J.-K. Lee, A. Goyal, Heteroepitaxial Cu2O thin film solar cell on metallic substrates, Sci. Rep. 5 (2015) 16272.

[9] D.S. Darvish, H.A. Atwater, Epitaxial growth of Cu2O and ZnO/Cu2O thin films on MgO by plasma-assisted molecular beam epitaxy, J. Cryst. Growth 319 (2011) 39–43.

[10] S. Dolai, S. Das, S. Hussain, R. Bhar, A. Pal, Cuprous oxide (Cu2O) thin films prepared by reactive d.c. sputtering technique, Vacuum 141 (2017) 296–306.

[11] M. Ottosson, J.-O. Carlsson, Chemical vapour deposition of Cu2O and CuO from CuI and O2 or N2O, Surf. Coatings Technol. 78 (1996) 263–273.

[12] D. Barreca, A. Gasparotto, E. Tondello, CVD Cu2O and CuO Nanosystems Characterized by XPS, Surf. Sci. Spectra 14 (2007) 41–51.

[13] C.R. Crick, I.P. Parkin, CVD of copper and copper oxide thin films via the in situ reduction of copper(ii) nitrate—a route to conformal superhydrophobic coatings, J. Mater. Chem. 21 (2011) 14712.

[14] A. El Kasmi, Z.-Y. Tian, H. Vieker, A. Beyer, T. Chafik, Innovative CVD synthesis of Cu2O catalysts for CO oxidation, Appl. Catal. B Environ. 186 (2016) 10–18.

[15] A.D. Handoko et al., Mechanistic Insights into the Selective Electroreduction of Carbon Dioxide to Ethylene on Cu 2 O-Derived Copper Catalysts, J. Phys. Chem. C 120 (2016) 20058–20067.

[16] A.E. Rakhshani, J. Varghese, Galvanostatic deposition of thin films of cuprous oxide, Sol. Energy Mater. 15 (1987) 237–248.

[17] A.E. Rakhshani, J. Varghese, Surface texture in electrodeposited films of cuprous oxide, J. Mater. Sci. 23 (1988) 3847–3853.

[18] W. Siripala, Study of annealing effects of cuprous oxide grown by electrodeposition technique, Sol. Energy Mater. Sol. Cells 44 (1996) 251–260.

[19] S.L. Marchiano, C.I. Elsner, A.J. Arvia, The anodic formation and cathodic reduction of cuprous oxide films on copper in sodium hydroxide solutions, J. Appl. Electrochem. 10 (1980) 365–377.

[20] I.S. Brandt, M.A. Tumelero, S. Pelegrini, G. Zangari, A.A. Pasa, Electrodeposition of Cu2O: growth, properties, and applications, J. Solid State Electrochem. 21 (2017) 1999–2020.

[21] M.J. Siegfried, K.-S. Choi, Elucidating the Effect of Additives on the Growth and Stability of Cu 2 O Surfaces via Shape Transformation of Pre-Grown Crystals, J. Am. Chem. Soc. 128 (2006) 10356–10357.

[22] P.E. de Jongh, D. Vanmaekelbergh, J.J. Kelly, Cu2O: Electrodeposition and Characterization, Chem. Mater. 11 (1999) 3512–3517.

[23] W. Zhao et al., Electrodeposition of Cu2O films and their photoelectrochemical properties, CrystEngComm 13 (2011) 2871.

[24] P. Wang, H. Wu, Y. Tang, R. Amal, Y.H. Ng, Electrodeposited Cu2O as Photoelectrodes with Controllable Conductivity Type for Solar Energy Conversion, J. Phys. Chem. C 119 (2015) 26275–26282.

[25] T.D. Golden et al., Electrochemical Deposition of Copper(I) Oxide Films, Chem. Mater. 8 (1996) 2499–2504.

[26] K.D.R.N. Kalubowila et al., Effect of Bath pH on Electronic and Morphological Properties of Electrodeposited Cu 2 O Thin Films, J. Electrochem. Soc. 166 (2019) D113–D119.

[27] W.M. Heijboer et al., Kβ-detected XANES of framework-substituted FeZSM-5 zeolites, J. Phys. Chem. B 108 (2004) 10002–10011.

[28] T. Günter, D.E. Doronkin, H.W.P. Carvalho, M. Casapu, J.D. Grunwaldt, HERFD-XANES and XES as complementary operando tools for monitoring the structure of Cu-based zeolite catalysts during NOx-removal by ammonia SCR, J. Phys. Conf. Ser. 712 (2016).

[29] M. Pashchanka et al., A molecular approach to Cu doped ZnO nanorods with tunable dopant content, Dalt. Trans. 40 (2011) 4307–4314.

[30] W. Septina et al., Potentiostatic electrodeposition of cuprous oxide thin films for photovoltaic applications, Electrochim. Acta 56 (2011) 4882–4888.

[31] S. Hayama et al., The scanning four-bounce monochromator for beamline I20 at the Diamond Light Source, J. Synchrotron Radiat. 25 (2018) 1556–1564.

[32] B. Ravel, M. Newville, ATHENA, ARTEMIS, HEPHAESTUS : data analysis for X-ray absorption spectroscopy using IFEFFIT, J. Synchrotron Radiat. 12 (2005) 537–541.

[33] J.-N. Nian, C.-C. Tsai, P.-C. Lin, H. Teng, Elucidating the Conductivity-Type Transition Mechanism of p-Type Cu2O Films from Electrodeposition, J. Electrochem. Soc. 156 (2009) H567–H573.

[34] D. Powell, A. Compaan, J.R. Macdonald, R.A. Forman, Raman-scattering study of ion-implantation-produced damage in Cu2O, Phys. Rev. B 12 (1975) 20–25.

[35] G. Niaura, Surface-enhanced Raman spectroscopic observation of two kinds of adsorbed OH− ions at copper electrode, Electrochim. Acta 45 (2000) 3507–3519.

[36] Y. Deng, A.D. Handoko, Y. Du, S. Xi, B.S. Yeo, In Situ Raman Spectroscopy of Copper and Copper Oxide Surfaces during Electrochemical Oxygen Evolution Reaction: Identification of Cu III Oxides as Catalytically Active Species, ACS Catal. 6 (2016) 2473–2481.

[37] J. Ferraro, K. Nakamoto, C.W. Brown, Introductory Raman Spectroscopy, Academic Press, 2003.

[38] B.K. Meyer et al., Binary copper oxide semiconductors: From materials towards devices, Phys. status solidi 249 (2012) 1487–1509.

[39] C. Wang et al., Structural, optical and photoelectrical properties of Cu2O films electrodeposited at different pH, RSC Adv. 6 (2016) 4422–4428.

[40] M.C. Biesinger, L.W. Lau, A.R. Gerson, R.S.C. Smart, Resolving surface chemical states in XPS analysis of first row transition metals, oxides and hydroxides: Sc, Ti, V Cu and Zn, Appl. Surf. Sci. 257 (2010) 887–898.

[41] L. Kundakovic, M. Flytzani-Stephanopoulos, Reduction characteristics of copper oxide in cerium and zirconium oxide systems, Appl. Catal. A Gen. 171 (1998) 13–29.

[42] F. Li, L. Zhang, D.G. Evans, X. Duan, Structure and surface chemistry of manganese-doped copper-based mixed metal oxides derived from layered double hydroxides, Colloids Surf. A Physicochem. Eng. Asp. 244 (2004) 169–177.

[43] P. Velásquez et al., A Chemical, Morphological, and Electrochemical (XPS, SEM/EDX, CV, and EIS) Analysis of Electrochemically Modified Electrode Surfaces of Natural Chalcopyrite (CuFeS2) and Pyrite (FeS2) in Alkaline Solutions, J. Phys. Chem. B 109 (2005) 4977–4988.

[44] L. Meda, G.F. Cerofolini, A decomposition procedure for the determination of copper oxidation states in Cu-zeolites by XPS, Surf. Interface Anal. 36 (2004) 756–759.

[45] M.C. Biesinger, Advanced analysis of copper X-ray photoelectron spectra, Surf. Interface Anal. 49 (2017) 1325–1334.

[46] S. Poulston, P.M. Parlett, P. Stone, M. Bowker, Surface Oxidation and Reduction of CuO and Cu2O Studied Using XPS and XAES, Surf. Interface Anal. 24 (1996) 811–820.

[47] G. Deroubaix, P. Marcus, X-ray photoelectron spectroscopy analysis of copper and zinc oxides and sulphides, Surf. Interface Anal. 18 (1992) 39–46.

[48] A. Gaur, B.D. Shrivastava, S.K. Joshi, Copper K-edge XANES of Cu(I) and Cu(II) oxide mixtures, J. Phys. Conf. Ser. 190 (2009) 012084.

[49] J. Rudolph, C.R. Jacob, Revisiting the Dependence of Cu K-Edge X-ray Absorption Spectra on Oxidation State and Coordination Environment, Inorg. Chem. 57 (2018) 10591–10607.

[50] J. Keating, G. Sankar, T.I. Hyde, S. Kohara, K. Ohara, Elucidation of structure and nature of the PdO-Pd transformation using in situ PDF and XAS techniques, Phys. Chem. Chem. Phys. 15 (2013) 8555–8565.

[51] K.A. Lomachenko et al., The Cu-CHA deNOx Catalyst in Action: Temperature-Dependent NH3-Assisted Selective Catalytic Reduction Monitored by Operando XAS and XES, J. Am. Chem. Soc. 138 (2016) 12025–12028.

[52] J. Liang et al., Reactivity and Transformation of Antimetastatic and Cytotoxic Rhodium(III)-Dimethyl Sulfoxide Complexes in Biological Fluids: An XAS Speciation Study, Inorg. Chem. 58 (2019) 4880–4893.

[53] S. Calvin, XAFS for Everyone, CRC Press, 2013.

[54] A.R. Denton, N.W. Ashcroft, Vegard's law, Phys. Rev. A 43 (1991) 3161–3164.

[55] L. Dupont, E. Guillon, J. Bouanda, J. Dumonceau, M. Aplincourt, EXAFS and XANES Studies of Retention of Copper and Lead by a Lignocellulosic Biomaterial, Environ. Sci. Technol. 36 (2002) 5062–5066.

[56] K.I. Shimizu, H. Maeshima, H. Yoshida, A. Satsuma, T. Hattori, Ligand field effect on the chemical shift in XANES spectra of Cu(II) compounds, Phys. Chem. Chem. Phys. 3 (2001) 862–866.

[57] A. Gaur et al., Identification of different coordination geometries by XAFS in copper(II) complexes with trimesic acid, J. Mol. Struct. 1121 (2016) 119–127.

[58] V. Petkov et al., Deviations from Vegard's law and evolution of the electrocatalytic activity and stability of Pt-based nanoalloys inside fuel cells by: In operando X-ray spectroscopy and total scattering, Nanoscale 11 (2019) 5512–5525.

[59] M.L. Baker et al., K- and L-edge X-ray absorption spectroscopy (XAS) and resonant inelastic X-ray scattering (RIXS) determination of differential orbital covalency (DOC) of transition metal sites, Coord. Chem. Rev. 345 (2017) 182–208.

[60] A. Gaur, B.D. Shrivastava, Speciation using X-ray absorption fine structure (XAFS), Rev. J. Chem. 5 (2015) 361–398.

[61] Y. Zhao et al., Epitaxial growth of hyperbranched Cu/Cu2O/CuO core-shell nanowire heterostructures for lithium-ion batteries, Nano Res. 8 (2015) 2763–2776.

[62] S.W. Donne, F.H. Feddrix, R. Glöckner, S. Marion, T. Norby, Water and protons in electrodeposited MnO2 (EMD), Solid State Ionics 152–153 (2002) 695–701.

[63] M. Sano, S. Komorita, H. Yamatera, XANES spectra of copper(II) complexes: correlation of the intensity of the 1s to 3d transition and the shape of the complex, Inorg. Chem. 31 (1992) 459–463.

[64] K. Kervinen et al., Zeolite framework stabilized copper complex inspired by the 2-His-1-carboxylate facial triad motif yielding oxidation catalysts, J. Am. Chem. Soc. 128 (2006) 3208–3217.

[65] R. Zhang, J.S. McEwen, Local Environment Sensitivity of the Cu K-Edge XANES Features in Cu-SSZ-13: Analysis from First-Principles, J. Phys. Chem. Lett. 9 (2018) 3035–3042.

[66] E.M.C. Alayon, M. Nachtegaal, E. Kleymenov, J.A. Van Bokhoven, Determination of the electronic and geometric structure of Cu sites during methane conversion over Cu-MOR with X-ray absorption spectroscopy, Microporous Mesoporous Mater. 166 (2013) 131–136.

[67] T. Schedel-Niedrig et al., Copper (sub)oxide formation: A surface sensitive characterization of model catalysts, Phys. Chem. Chem. Phys. 2 (2000) 2407–2417.

[68] A. Kuzmin, J. Chaboy, EXAFS and XANES analysis of oxides at the nanoscale, IUCrJ 1 (2014) 571–589.

[69] A. Wells, Structural Inorganic Chemistry, Clarendon Press, Oxford, 1984.

[70] S. Åsbrink, L.J. Norrby, A refinement of the crystal structure of copper(II) oxide with a discussion of some exceptional e.s.d's., Acta Crystallogr. Sect. B Struct. Crystallogr. Cryst. Chem. 26 (1970) 8–15.

[71] X. Guo et al., CuO/Pd composite photocathodes for photoelectrochemical hydrogen evolution reaction, Int. J. Hydrogen Energy 39 (2014) 7686–7696.

[72] S. Ho-Kimura, S.J.A. Moniz, J. Tang, I.P. Parkin, A method for synthesis of renewable Cu2O junction composite electrodes and their photoelectrochemical properties, ACS Sustain. Chem. Eng. 3 (2015) 710–717.

[73] C.Y. Chiang, M.H. Chang, H.S. Liu, C.Y. Tai, S. Ehrman, Process intensification in the production of photocatalysts for solar hydrogen generation, Ind. Eng. Chem. Res. 51 (2012) 5207–5215.

[74] Y. Yang, D. Xu, Q. Wu, P. Diao, Cu2O/CuO bilayered composite as a high-efficiency photocathode for photoelectrochemical hydrogen evolution reaction, Sci. Rep. 6 (2016) 1–13.

[75] E. Pastor et al., Spectroelectrochemical analysis of the mechanism of (photo)electrochemical hydrogen evolution at a catalytic interface, Nat. Commun. 8 (2017).

[76] A.D. Handoko, J. Tang, Controllable proton and CO2 photoreduction over Cu2O with various morphologies, Int. J. Hydrogen Energy 38 (2013) 13017–13022.

[77] J. Di et al., Ultrathin two-dimensional materials for photo- and electrocatalytic hydrogen evolution, Mater. Today 21 (2018) 749–770.

[78] C.S. Chen et al., Stable and selective electrochemical reduction of carbon dioxide to ethylene on copper mesocrystals, Catal. Sci. Technol. 5 (2015) 161–168.